SUPPORTING INFORMATION

Thallium sorption by soil manganese oxides: Insights from synchrotron X-ray micro-analyses on a naturally thallium-rich soil

Francesco Femi Marafatto[*,+], Rainer Dähn[*], Daniel Grolimund[°], Jörg Göttlicher[#], Andreas Voegelin[+]

[*] Paul Scherrer Institute, Laboratory of Waste Management, Forschungstrasse 111, Villigen PSI, CH-5232 (Switzerland)

[°] Paul Scherrer Institute, Swiss Light Source, microXAS beamline, Forschungstrasse 111, Villigen PSI, CH-5232 (Switzerland)

[+] Eawag, Department of Water Resources and Drinking Water, Ueberlandstrasse 133, Dübendorf, CH-8600 (Switzerland)

[#] Karlsruhe Institute of Technology, Institute for Photon Science and Synchrotron Radiation, KIT Campus North, Hermann-von-Helmholtz-Platz 1, Eggenstein-Leopoldshafen, D-76344 (Germany)

1. Laboratory μ-XRF data

Two 10×10 mm^2 thin-sections of the soil PI 38 were analysed on a laboratory μ-XRF instrument at a spatial resolution of ~20 μm (M4 Tornado, Bruker Nano GmbH). The instrument was equipped with an Ag X-ray tube for sample excitation, polycapillary X-ray optics for beam focusing, and two Si drift detectors for fluorescence detection. Figure S1 shows selected results for the section analysed in detail at beamlines SUL-X and I18.

Using the autophase algorithm implemented in the instrument software Esprit, the Fe, Mn and Tl count intensity maps were evaluated to extract a phase map which differentiated three major phases: soil matrix (P1), voids/cracks (P2) and Mn- and Tl-rich concretions (P3). The spectrum of the phase P3 was evaluated by the fundamental parameter quantification routine implemented in the instrument software. From the normalized atomic concentrations, a molar Tl/Mn ratio of 0.0066 was calculated for the Tl- and Mn-rich concretions phase. The analogous analysis of a second section returned very similar results, with a molar Tl/Mn ratio of 0.0063 for the Tl- and Mn-rich concretions phase (not shown).

The positions on which XANES spectra on selected points of interest (POI) were recorded at SUL-X and chemical imaging over selected regions of interest (ROI) was performed at I18 are also shown in Figure S1. The XRF spectra collected over the green-marked rectangular areas were evaluated with the semiquantitative fundamental parameter method. The resulting molar Tl/Mn ratios were used to derived scaling factors to derive estimates of molar Tl/Mn ratios from synchrotron-derived Tl/Mn count ratios (Table S1).
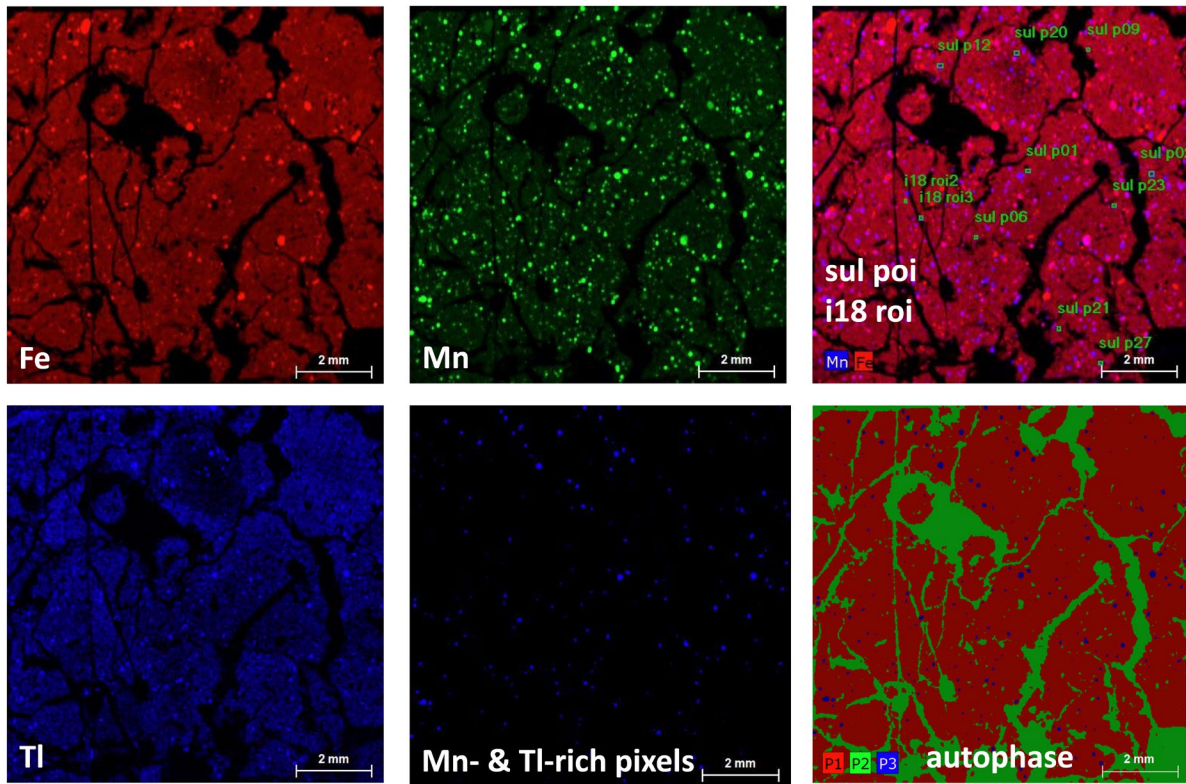
Figure S1: Element distribution maps for Fe, Mn, and Tl, map of Mn- and Tl-rich pixels (phase P3) identified with the autophase algorithm of the Bruker Esprit software, autophase map for P1 (soil matrix), P2 (resin/voids) and P3 (Tl- and Mn-rich phase) and map showing spots where point XANES data were collected at SUL-X and chemical imaging of individual concretions was evaluated at I18. Note: the vertical crack in the left part of the section formed when the section was removed from the sample holder at I18, before analysis of the section at SUL-X and the re-analysis on the laboratory instrument.
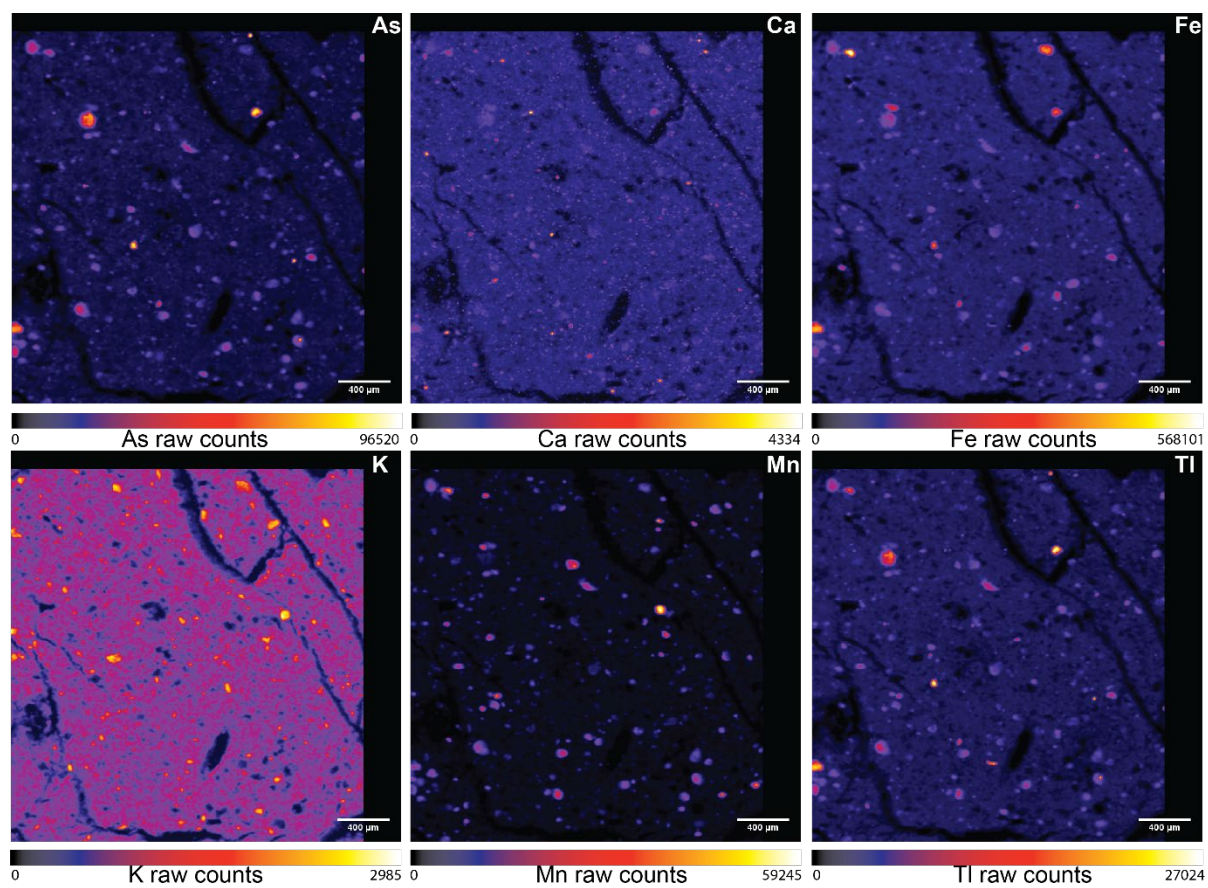
Figure S2: Multipanel figure showing elemental distribution from the data collected at I18 at Diamond.

Table S1: Comparison between the Tl/Mn count ratios derived from XRF data collected at the SUL-X and I18 beamlines with molar Tl/Mn ratios obtained from laboratory micro-XRF data using a semi-quantitative fundamental parameter (M4 Tornado instrument with Esprit software, Bruker Nano GmbH). The average ratios between the two measurements were evaluated to be 0.13 (SUL-X) and 10. (I18). These ratios were used as correction factors on the synchrotron-derived Tl counts to obtain corrected Tl/Mn count ratios that were close to expected molar Tl/Mn ratios. Corrected Tl counts and Tl/Mn count ratios are shown in Figures 1 through 5.

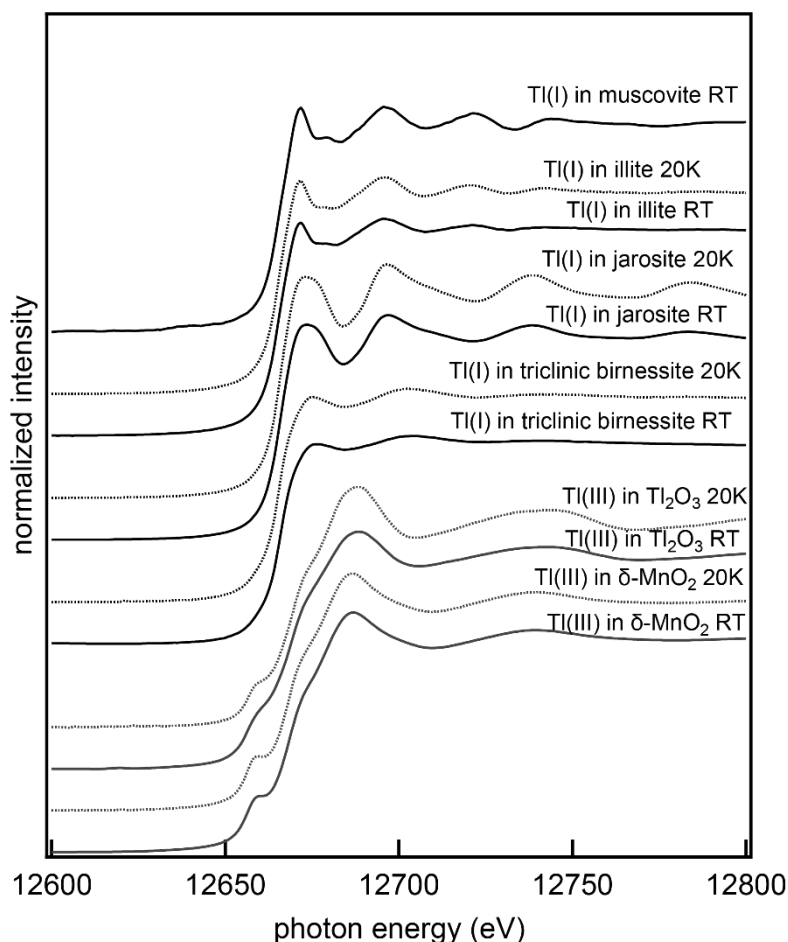| Datapoint	Beamline	Tornado	Ratio
beamline SUL-X			
POI 12	0.091	0.0117	0.128
POI 20	0.063	0.0086	0.137
POI 02	0.062	0.0080	0.129
POI 09	0.029	0.0076	0.266
POI 23	0.058	0.0061	0.105
POI 21	0.036	0.0036	0.100
POI 01	0.046	0.0012	0.025
		average	**0.13**
		st. dev	**0.07**
beamline I18			
ROI 2	0.0022	0.0003	7
ROI 3	0.0112	0.0009	13
		average	**10**
		st. dev	**4**

2. Synchrotron data

Figure S3. Reference spectra used to fit the data in this manuscript, separated by oxidation state (lower oxidation state below) and temperature at which they were measured (gray at 20 K, black at room temperature – RT). Spectra recorded at RT were used to evaluate the XANES spectra collected at the SUL-X beamline, spectra recorded at 20 K were used to evaluate the chemical imaging data collected at the I18 beamline.

2.1 XRF map derivation

XRF maps collected at 15 keV and saved in hdf5 format were loaded in PyMCA, where I0 was divided automatically from the data, and then batch fitting was performed pixelwise to obtain tiff images of deconvoluted counts for each selected element after calibrating the spectrum from channels to energies. The fit parameters for the MCA fit in PyMCA were left as default except for the excitation energy and the background stripping, pile-up peaks, scattering peaks and short tail peaks were included after visual inspection of the fit. The simplified approach was deemed sufficient since all we were looking for were deconvoluted peaks.

The data collected at the I18 beamline was organized in nexus hdf5 files (*.nxs), where all acquisition parameters, positions of motors, beamline settings and the measurements of all detectors at every point were organized in a preset data tree defined by the Diamond lightsource which changes with beamline variations. This data had to first be reduced to tiff images in order to be both observable with an image analysis program and processed with the python programming language.

2.2 Python data processing code

Data processing of the chemical imaging XRF maps collected at different energies at I18 as well as the method validation with the point XANES from SUL-X was performed with 3 python scripts (written for python 3.6), in order to obtain the speciation of Tl for every pixel as well as to perform background subtraction and correlation of Tl with Mn. All scripts are structured in five parts: (i) description of tasks performed by script; (ii) loading of libraries; (iii) space for user input (folder names, optional parameters); (iv) definitions of functions; and (v) actual code. All scripts are of publicly availability at https://doi.org/10.25678/0002XK

2.2.1 Script 1

The first script extracted the data from the hdf5 containers and saved it as tiff images in folders based on incoming energy and measured element. The user needs to provide the directory in which the data was saved from the diamond fileserver. The structure of the diamond data is that for each map there is one rawfile, one "pandafile" and one "processed" file. All three are required for the script to run, and they should be in the same folder structure as they were saved into. The script will then read all the hdf5 files for each measurement, in particular the data (full spectrum and element-specific multichannel analyzer (MCA) counts)), the monochromator energy, the name of the sample as assigned in the measurement and the encoder X and Y values. It will then evaluate from the rawfile the filename and the energy at which the measurement was done and create a folder made of the original filename and energy. Inside this folder, there will be two subfolders: one to contain the element MCA tiff files, a second to contain the tiff files for the full spectra (one tiff file per channel). These images can for example be loaded in PyMCA (even though this is redundant, since PyMCA can already read the nexus hdf5 files). During file reading, there was an issue that was observed in some cases and this regarded maps that were recorded in "snake" mode. In such cases, and non-reproducibly, the measurement in snake mode resulted in a zigzag issue by which the motors were skipping one position every other line. A function was written to correct this, and it can be enabled or disabled in the script. Once the files have been read and folders have been created,

the script will take each image and divide it by the value of I$_0$. The Diamond lightsource operates in top-up mode, but nevertheless there is a 1% variation in incoming flux, which is worth correcting to minimize noise where possible (Mosselmans et al., 2009). Finally, this script will save the data as tiff files in the correct folders in a way that the second script can read them. Additionally, it will save a text file with the X and Y encoder values (the positions of the motors). This is to facilitate the alignment of images in the following script.

2.2.2 Script 2

The second script is designed to operate on the images generated by srcipt 1 in order to provide chemical speciation information. It will read in a folder with a sample name, which contains subfolders each named with the energy at which the containing maps were recorded (as described for script 1).

The main parameters that can be selected in this script are: the input folder for the sample; the input folders containing the normalized spectra from Athena for the oxidized species and the reduced species; whether to select or not regions of interest (ROI) in the data; whether to reduce the data with a moving average and the size of the moving average window; whether to mask the element of choice based on the edge step; the elements to read in (one for the alignment, one for the chemical redox maps and one as denominator if correlations need to be made); whether to use the highest energy in the chemical maps or another one (i.e. 15 keV) as reference for the ratio values (for a semiquantitative comparison); the values for the attenuation if for example a Z-1 filter was used on the detector (transmittance values calculated using Hephaestus (Ravel and Newville, 2005)), or just the molecular weights of the elements measured, or finally a scaling factor if no correction can be made but an external calibration has been performed. The functions defined just below operate different purposes in the scripts. The remaining functions create folders, simplify some mathematical operations, or operate on images and are self-explanatory. A function named "ROIs" allows the user to select square regions of interest from the map, and then will split the map in all these datasets and operate everything that follows on each of these individual ROIs independently. If none are selected, it will run the full map as if it were one single ROI. If in the root folder there is a file called "roi_coordinates.csv" that contains rows of lists containing coordinates (starting x coordinate, starting y coordinate, width of the ROI in pixels, height of the ROI in pixels). If it is present, it will read it. This function will save the "roi_coordinates.csv" file as well as two images with the ROIs drawn upon them. The two images chosen are the ratio map as well as the individual elements normalized by their respective maximum intensity. The following function, pixelLCF, will

operate the least squares fitting of the data to 1 reference for every pixel. It will read for every pixel the values at each energy, compare them with each reference from the list running the least squares algorithm (Stark and Parker, 1995) constraining the value of the fit between 0 and 1. It will then output the result as well as the relative net sum of squared residuals (NSSR). The function pixel_2compLCF operates similarly, with the only difference that it will select 2 references to do a 2 component fit. The output will be the fitted values and the NSSR matrix for each. The last function for the fitting, LCF_sel, will perform the actual selection of the values in the arrays created previously by only selecting the values that had the lowest NSSR.

The script then reads the data, aligns the images and operates the moving average on the aligned images. In the first case, it will check whether the grid value is present. This grid value is used to resize the images that are smaller (i.e. if for some reason one of the images was sampled with a larger stepsize than the others) to the other images in the stack. The alignment is performed with the phase_cross_correlation algorithm of the python scikit library (Guizar-Sicairos et al., 2008). The script will then read the references and read the values at which the energy maps were acquired. The following section normalizes the data of the chemical maps so that the counts are converted in a scale that is comparable to that of the references read in, which makes the linear squares fitting possible. It will then proceed by selecting the ROIs based on the functions described previously. A loop follows in which the script will operate for every ROI selected on the maps. At this point, the xlsx output will be populated with a summary of all the calculations that have been done. In particular, the first spreadsheet will contain a list of references as well as a number for each reference as a legend for the resulting images. A second spreadsheet will list all pixels in tabled form, in order to perform correlations or other graphical analysis, and in particular the Tl, Mn and As MCA counts will be given as well as the raw Tl/Mn count ratio or the one scaled by the corrective factor identified in table S1, and a column with the normalized Tl(III) amount. The last two columns show the references that were chosen for the LCF. The third spreadsheet will show the averages for all pixels for each energy, in order to be able to plot an average spectrum of the area. In the case of ROI selection, these spreadsheets are replicated for each roi in the output file. Finally, the script will save the output images as follows: an RGB image where every pixel is red for reduced and blue for oxidized; a similar image but where values are scaled by the numerator value in each pixel; analogously for the denominator; a series of images where the fit choices are given in a numerical scale both for the 1 and the 2 component fit as well as the NSSR values (a guide for this is present in the first spreadsheet of the output); an image with the selected fits based on the NSSR; an

image where the numerator and denominator maps are plotted in red and blue, respectively, and similarly but scaled to the numerator and to the denominator values.

2.2.3 Script 3

The third script had the purpose of reading the point XANES collected at SULX measured at selected points after they were background subtracted in Athena (Ravel and Newville, 2005) and saved as normalized spectra, and performing the least squares fitting of the data with references similarly as in the previously described code. The parameters given to the script are: the path to the point XANES hdf5 files and the paths to the normalized references for the oxidized and reduced species. Similarly as in the previous scripts, the attenuation factors for the different elements are calculated if the option is selected. The remaining lines of the script input section define the font to use for the labeling of the point XANES. The script will then read the normalized XANES files, as well as the references. The fitting of the XANES spectrum to the references is done similarly to the previous script with the least squares approach, selecting the 1 or 2 component fit if the 2 component NSSR is less than 80% of the 1 component fit. The results of the script are saved as an excel file where each scan contains: the references used for the 1 and 2 component fit, the percentage of oxidized species (normalized to 1 from the values of the 2 component fit) and a boolean specifying whether the 2 component is better than the 1 component fit. The Tl, Mn and As MCA counts are evaluated from the data saved in the point XANES of the hdf5 file. Then, the values for Tl were evaluated by subtracting an average within a range of energies below the edge from energies below the edge (12710 – 12730 eV and 12640 -12650 eV, respectively). As and Mn are evaluated as an average of the counts between 12710 and 12730 eV.
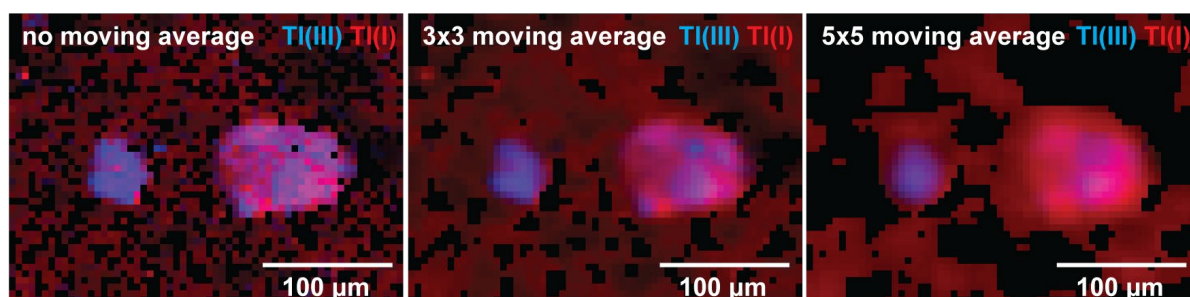

Figure S4: Effect of the moving average on the data. The black points are the masked areas according to the Tl edge step. The 3x3 moving average was deemed a good compromise, which reduced the noise in the data while still retaining information on the heterogeneities.
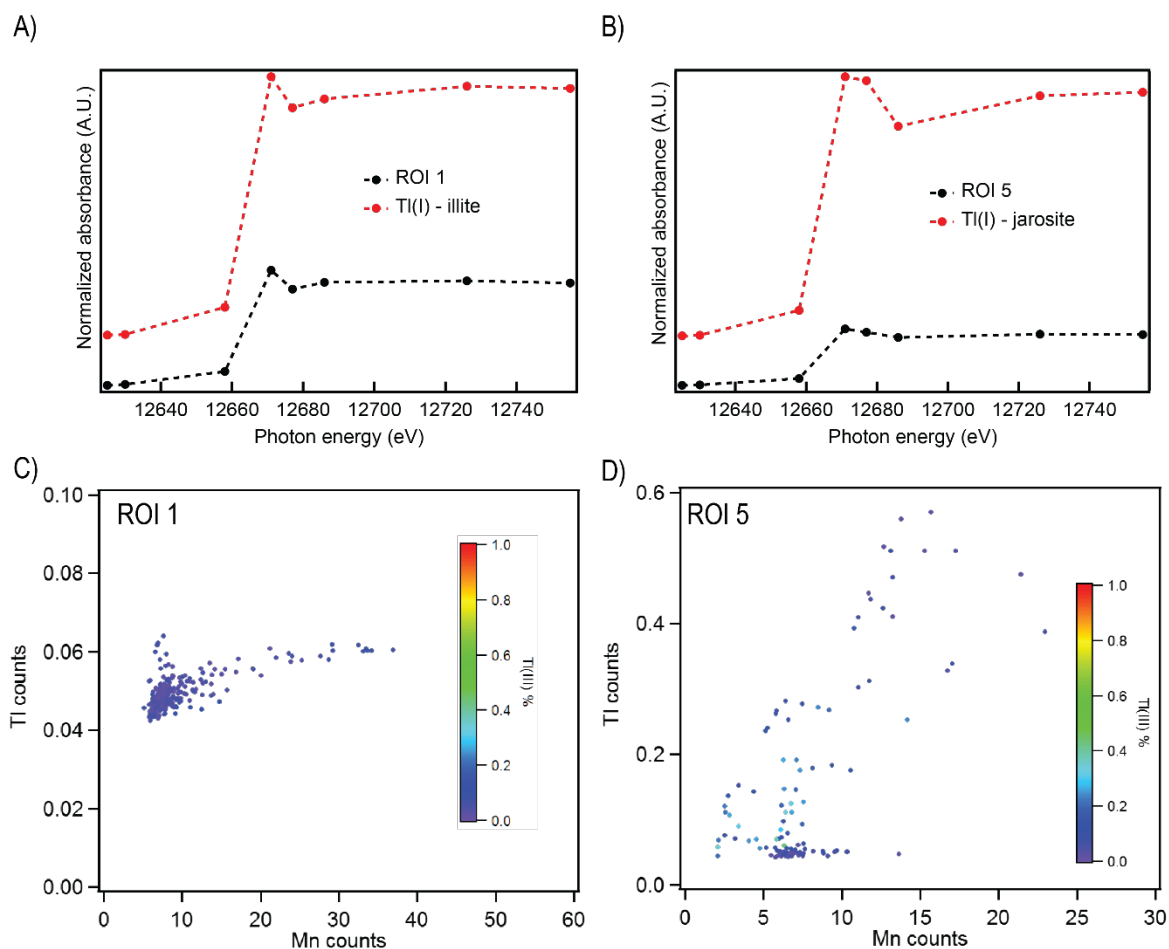
Figure S5: Tl vs Mn counts compared to the Tl average oxidation state for the pixels included in ROIs 1 (A, C) and 2 (B, D) identified in figure 2. ROI 1 was fit as Tl(I) in clays by the LCF script, ROI 2 was fit as Tl(I) in jarosite (inset).
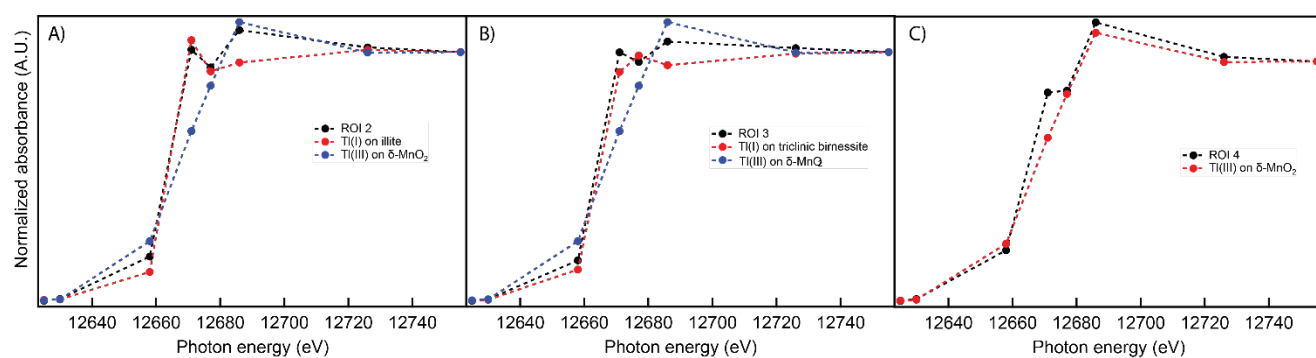

Figure S6: Average spectrum for ROIs 2 A), 3 (B) and 4 (C) compared with the major oxidation state fitted by the script.
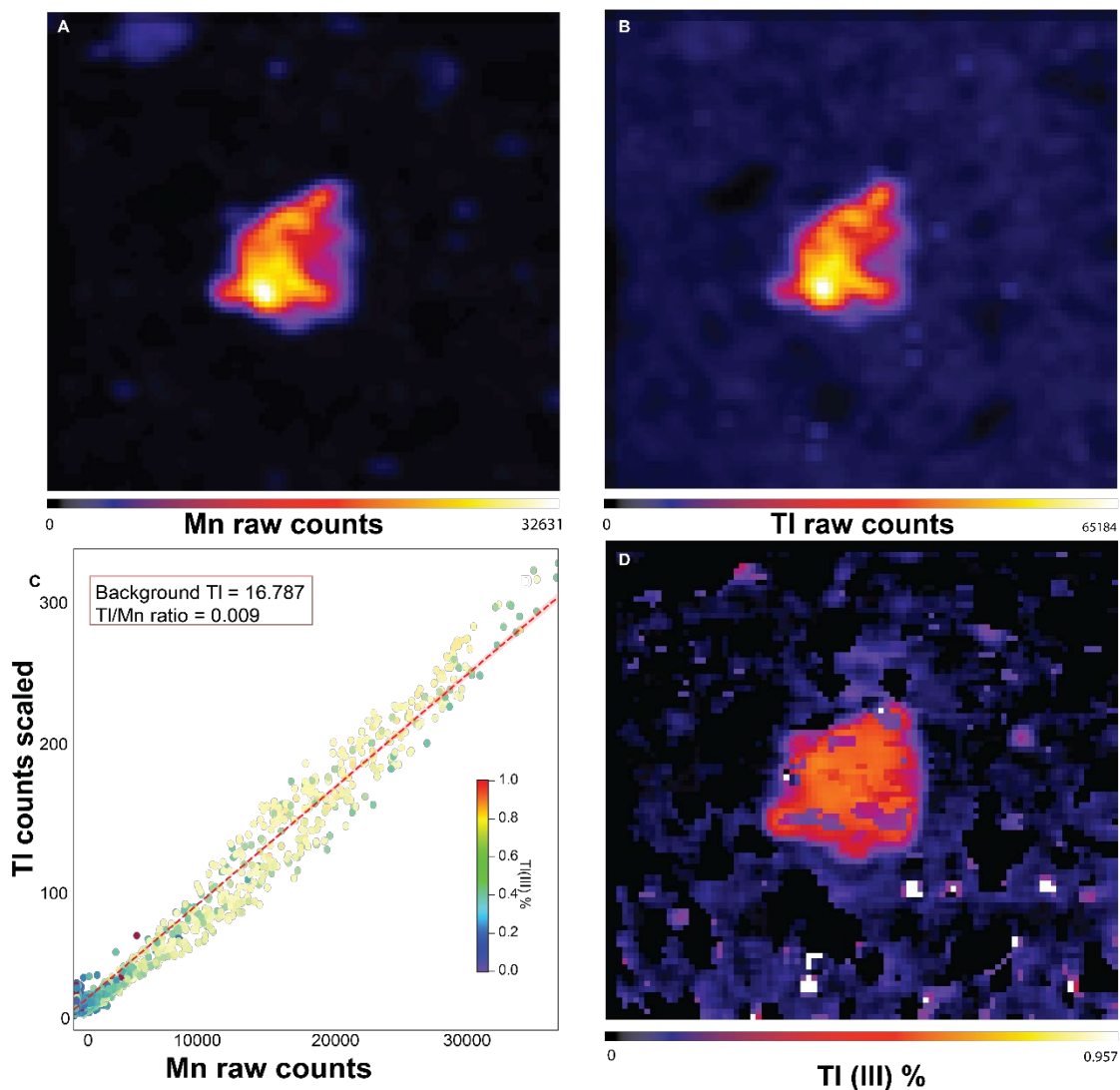
Figure S7: μ-XRF and chemical imaging data recorded with 5-μm X-ray beam at 10 K for a concretion on a thin section collected at a previous beamtime at I18. (A, B) Mn and Tl XRF maps collected at 15 keV over sub-area marked in red in Fig. 1. In terms of Tl(III) loading, as well as Tl/Mn ratio, this concretion is similar to ROI 2, although the absolute values are different because of different beamline settings at the time.In both maps, contrast adjusted to 80% of the maximum intensity. (C) Tl scaled counts (according to table S1) versus Mn raw counts, color-coded according to LCF-derived Tl(III) fraction. Lines depicting various molar Tl/Mn ratios are shown to guide the eye. (D) LCF-derived fraction of Tl(III) over mapped area, where black pixels indicate those masked out by the edge-step filter described in the text.

Table S2: Summary of the point XANES spectra acquired on the thin section measured at the SUL-X beamline, with positions marked in Figure 1C. The LCF resultsresults from the combinatorial LCF analysisin Athena (one scan at a time, including all references but limiting the maximum number of spectra in the fits to 2 and selecting the combination with the lowest R-factor). The Tl/Mn ratio was obtained from the XRF map at 15 keV deconvoluted with pyMCA for each point.

	MCA data			LCF results						
point	Tl counts scaled	Mn raw counts	Tl/Mn	Tl(III)-Tl$_2$O$_3$	Tl(III)-MnO$_2$	Tl(I)-illite	Tl(I)-muscovite	Tl(I)-MnO$_2$	Tl(I)-jarosite	R-factor
p01	4.51E-05	9.79E-03	4.61E-03		0.24	0.76				2.28E-03
p02	3.87E-04	6.19E-02	6.25E-03		0.36	0.65				8.58E-04
p03	6.77E-05	1.47E-02	4.59E-03		0.35	0.65				1.54E-03
p04	4.15E-05	1.58E-02	2.62E-03		0.11	0.90				7.51E-04
p05	3.91E-05	7.17E-03	5.45E-03		0.19	0.81				5.37E-04
p06	3.07E-04	1.50E-02	2.04E-02		0.83	0.17				4.89E-03
p07	6.90E-05	8.02E-03	8.60E-03		0.24	0.76				9.66E-04
p08	2.45E-05	4.28E-03	5.73E-03		0.29	0.71				9.99E-04
p09	5.11E-05	1.74E-02	2.93E-03		0.04	0.96				5.36E-04
p10	4.23E-05	4.64E-04	9.11E-02			0.40	0.60			7.31E-04
p11	3.18E-04	4.65E-04	6.83E-01			0.51	0.49			4.74E-04
p12	3.25E-04	3.58E-02	9.09E-03		0.60	0.40				2.16E-03
p13	2.24E-03	4.53E-03	4.94E-01				0.06		0.95	1.21E-03
p14	4.23E-04	3.12E-02	1.36E-02		0.25	0.75				2.99E-03
p15	3.72E-04	4.33E-03	8.58E-02				0.79	0.21		5.80E-03
p16	3.64E-04	3.95E-03	9.20E-02			0.53	0.48			9.89E-04
p17	3.97E-04	5.57E-03	7.13E-02			0.59	0.41			1.08E-03
p18	8.58E-04	2.21E-02	3.88E-02		0.53	0.47				5.12E-03
p19	5.69E-04	7.71E-02	7.38E-03		0.43	0.58				1.32E-03

	MCA data			LCF results

point	Tl counts scaled	Mn raw counts	Tl/Mn	Tl(III)-Tl$_2$O$_3$	Tl(III)-MnO$_2$	Tl(I)-illite	Tl(I)-muscovite	Tl(I)-MnO$_2$	Tl(I)-jarosite	R-factor
p20	2.25E-03	3.53E-01	6.39E-03		0.34	0.66				1.01E-03
p21	6.71E-04	1.80E-01	3.73E-03	0.08		0.92				1.04E-03
p22	2.59E-03	8.68E-02	2.98E-02		0.87	0.13				6.15E-03
p23	1.15E-03	1.93E-01	5.93E-03	0.26		0.74				1.47E-03
p24	8.73E-04	1.59E-01	5.50E-03		0.31	0.69				1.23E-03
p25	1.39E-03	4.01E-02	3.47E-02		0.68	0.32				3.85E-03
p26	7.05E-04	3.95E-03	1.79E-01				0.47		0.53	2.56E-03
p27	5.43E-04	1.26E-01	4.30E-03		0.29	0.71				1.19E-03
p28	3.75E-05	9.04E-04	4.15E-02	0.12		0.88				1.02E-02
p29	7.94E-04	1.20E-01	6.64E-03	0.30		0.70				1.37E-03
p30	5.35E-04	7.95E-02	6.72E-03		0.09	0.91				7.25E-04
p31	6.27E-05	5.58E-03	1.12E-02		0.29	0.71				1.64E-03
p32	7.53E-05	1.04E-02	7.23E-03		0.62	0.38				2.34E-03
p33	5.93E-05	7.06E-03	8.41E-03		0.24	0.76				1.18E-03
p34	6.85E-05	6.38E-03	1.07E-02		0.60	0.40				2.81E-03
p35	7.65E-05	3.60E-04	2.12E-01				0.26		0.74	8.75E-04
p36	5.18E-05	6.92E-04	7.48E-02				0.48		0.52	1.66E-03
p37	8.14E-05	7.14E-04	1.14E-01				0.10		0.90	2.59E-03
p38	1.12E-04	4.71E-04	2.38E-01		0.01				0.99	2.05E-04
p39	7.70E-05	2.74E-03	2.81E-02		0.07	0.93				1.27E-04
p40	6.52E-05	8.75E-03	7.45E-03		0.34	0.66				4.64E-04

3. Method validation

To validate the chemical imaging method against the traditional point XANES spectroscopy approach, two operations were carried out. In the first operation, we evaluated whether the python script-generated LCF was comparable to that performed by Athena, by processing the point XANES spectra collected at the SUL-X beamline with script 3 and comparing the results with those obtained with Athena. The results of this are shown in Figure S8, which confirms that the fitting algorithm (non-negative least squares with weights constrained between 0 and 1) was appropriate.
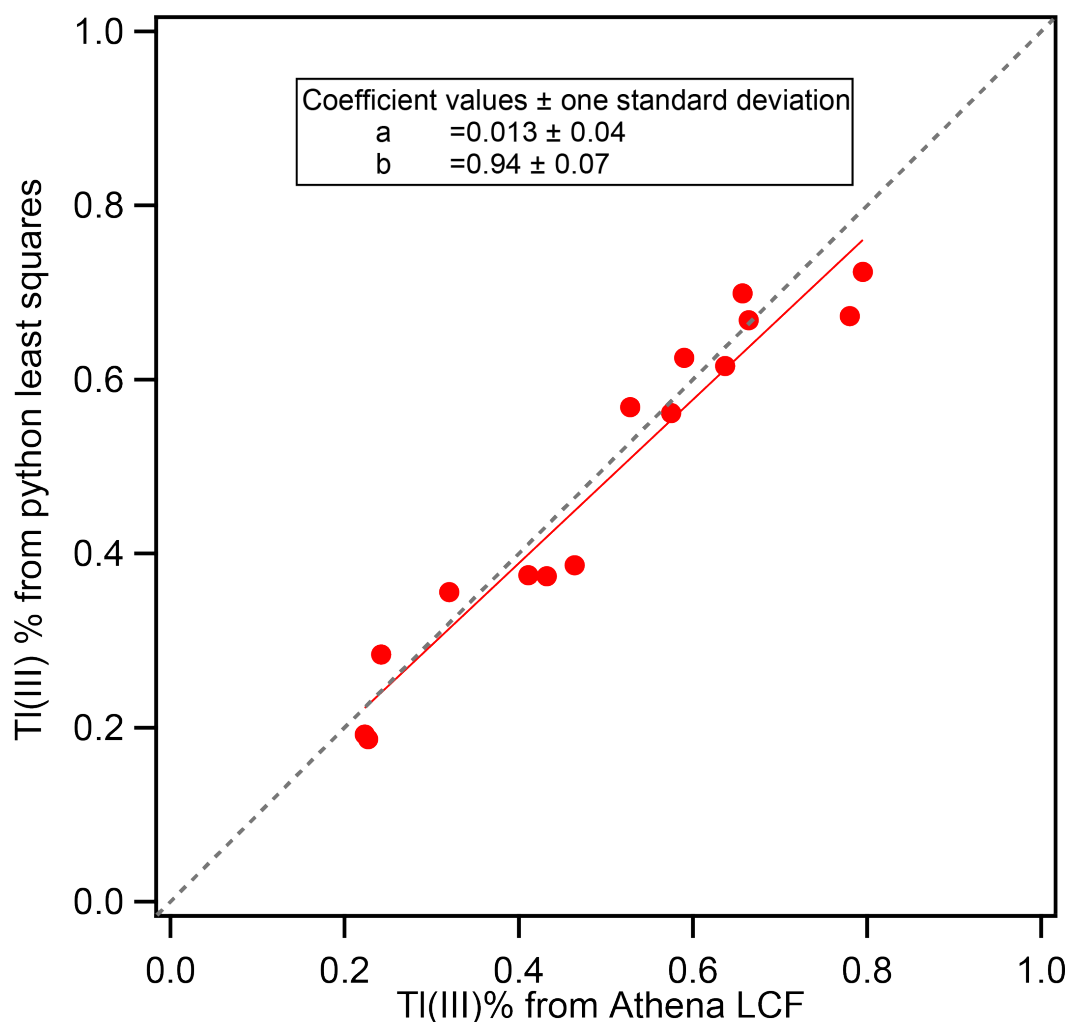

Figure S8: Correlation between the LCF procedure in Athena and the least squares performed with the python script for the point XANES spectra collected at SUL-X.

3.1 Uncertainty analysis for chemical imaging of the Tl redox speciation at I18

To assess the uncertainty of the Tl redox speciation derived from chemical imaging, we performed an uncertainty analysis as described in Wielinski et al. (2020). Briefly, a Bayesian inference model was developed and applied to the data to assess the impact of uncertainty on the interpretability of the chemical redox images collected at a limited amount of energies. In the applied model, the selection of 20'000 pixels by random permutation was performed 5 times on the dataset, and the results showed a Correct largest Spectral component identified (CSCI) of 76,31% with an increase in uncertainty of 4.55% compared to the previous run.

|	
Exclusion criteria:	All pixels that contained normalized X-ray absorption coefficients smaller -0.2 and larger 2 were eliminated. Otherwise, a few outliers significantly distorted the analysis.
Number of included pixels:	100'000 (29.01% of the total pixels). The first 100'000 pixels (starting left, moving right) that fulfilled the inclusion criteria were included in the analysis. In total, less than 5% of the pixels did not fulfill the inclusion criteria.
	An additional 20'000 pixels were sampled with random permutation 5 times, in a second run, and the uncertainty increased of only 4.55%
Uncertainty:	$0.0711 \pm 6.5685e\text{-}05$, Figure S9
Score, all refs:	0.650
Score, Tl(I) vs. Tl(III):	1.975 (not relevant)
Correct largest Spectral component identified (CSCI), all refs:	41.3%
CSCI, Tl(I) vs. Tl(III):	79.3%
Conclusion:	It can be estimated that in around 80% of the pixels, the dominant valence state is determined correctly.
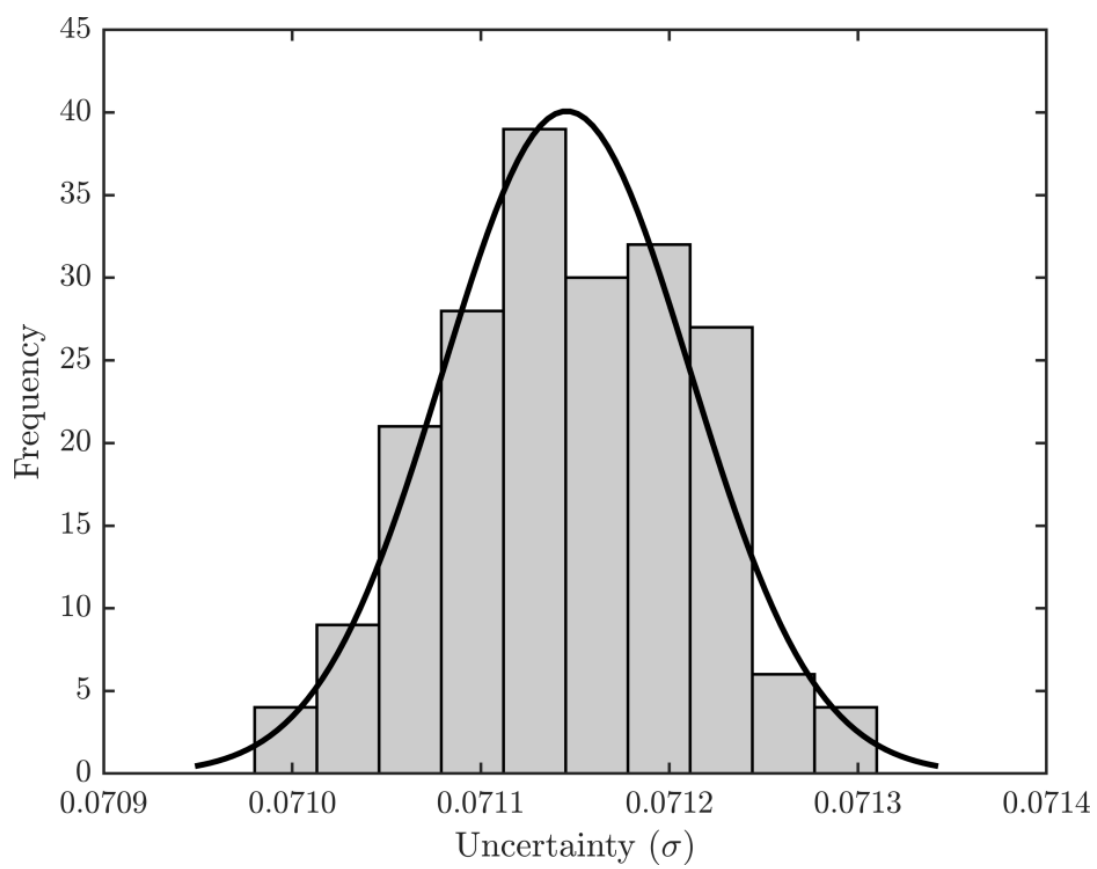
Figure S9: H for the dataset measured at I18

4. Reliability of the measurements with respect to radiation-induced speciation changes (beam damage).

4.1 SUL-X data

To evaluate whether the point XANES spectra recorded at SUL-X were affected by beam damage (since exposure at each scan was considerable and the sample was kept at room temperature) we replicated each scan 3 times and evaluated the three individual scans after aligning them to the reference Se foil. After verifying that the scans were not affected by beam damage (changes in edge shape and position), we merged them in energy. Of all 40 points measured, none showed evidence of beam damage within the 3 scans. An example of 3 individual scans for one point is shown in the top part of Figure S10.
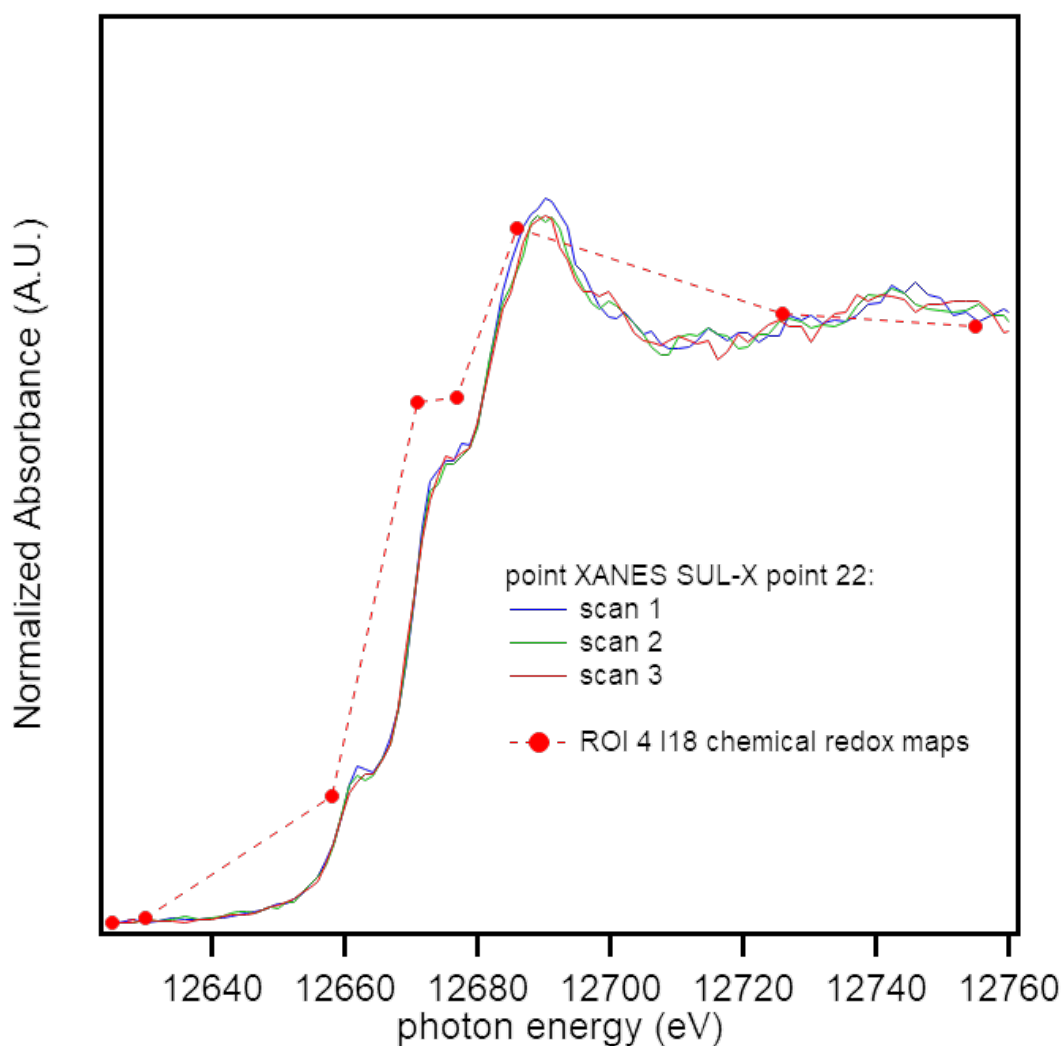

Figure S10: Comparison of data quality between the chemical maps (0.08 s), and the point XANES collected at SUL-X (5 min per scan).

4.2 I18 data

Radiation-induced changes in Tl (redox) speciation could not be excluded at the high flux density of the used at the I18 beamline, as evidenced by tests performed on Tl_2O_3 in a cellulose pellet that were performed at the microXAS beamline at the Swiss Light Source at comparable flux densities (Figure S11). To assess whether beam damage affected the chemical maps collected at I18, we collected chemical imaging maps on a single concretion (5 energies across Tl L_{III}-edge; with 200 ms integration time per pixel for each energy; i.e., 1 s/pixel for 5 energies). We then repeated the chemical imaging 4 more times with the same parameters, resulting in a total irradiation time per pixel of about 5 s. The data from the five chemical imaging stacks were processed with the python scripts to check for potential differences in the results with increasing total exposure time. For this, we plotted the Tl(III) fractions of the chemical imaging stacks 2 to 5 against the Tl(III) fractions from the first chemical imaging (Figure S12). The comparison showed some scatter in the data, which may also result from slight misalignment between the different imaging stacks. On the other hand, the correlation did not provide any evidence for substantial Tl reduction over a total of 5 s integration time per pixel. Also the visual comparison of the Tl(III) maps derived from the 5 chemical imaging stacks revealed no marked changes (Fig. S12), apart from a markedly higher noise level in the second stack which affected the respective results.
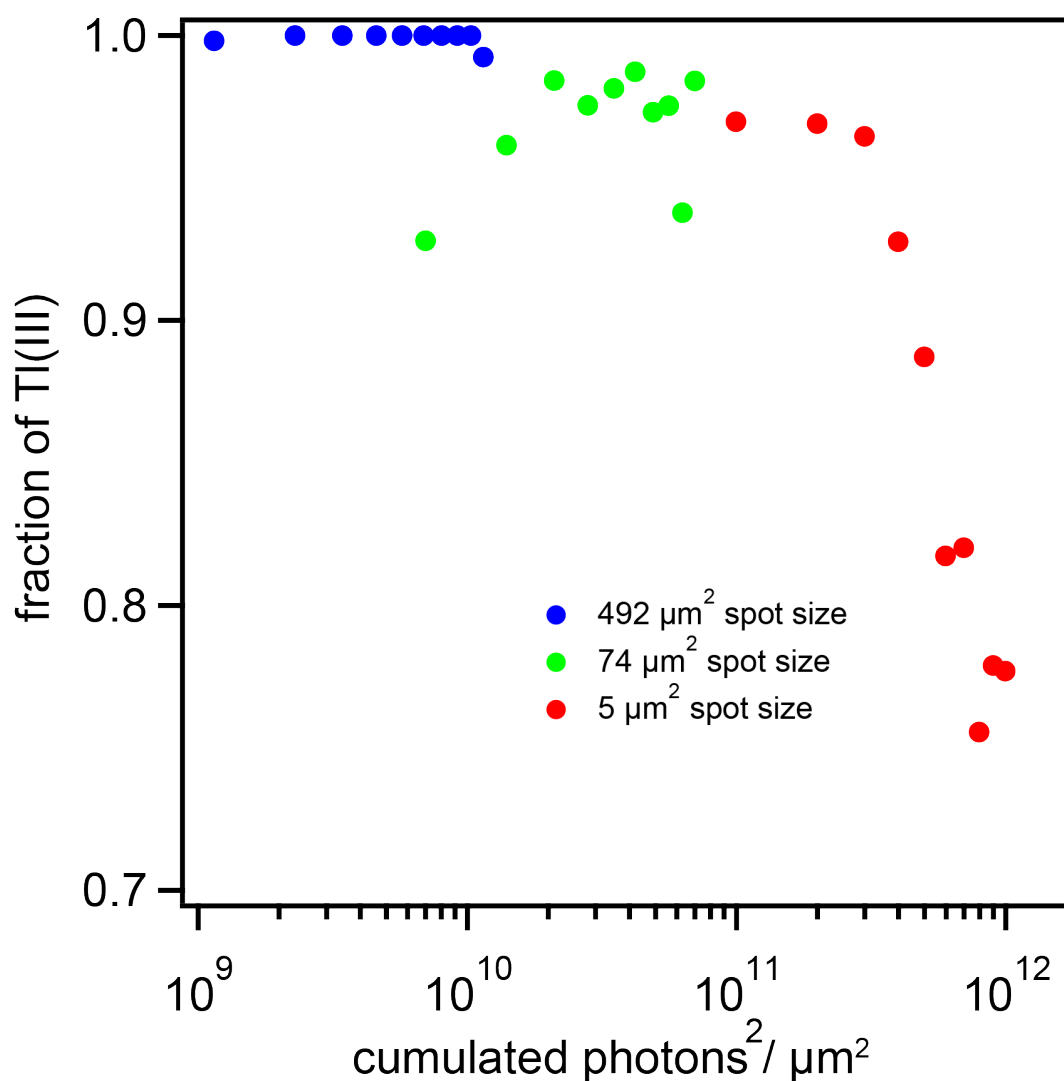
Figure S11: Test of radiation-induced reduction of Tl(III) in Tl_2O_3 in cellulose pellets at constant photon flux focused to different beam sizes (varying photon flux density) at temperature of 105 K. Each point is a single XANES scan of 4 minutes. The fraction of Tl(III) was estimated by LCF analysis (Athena). A smaller spot size and hence a higher photon flux density results in faster radiation-induced Tl(III) reduction.
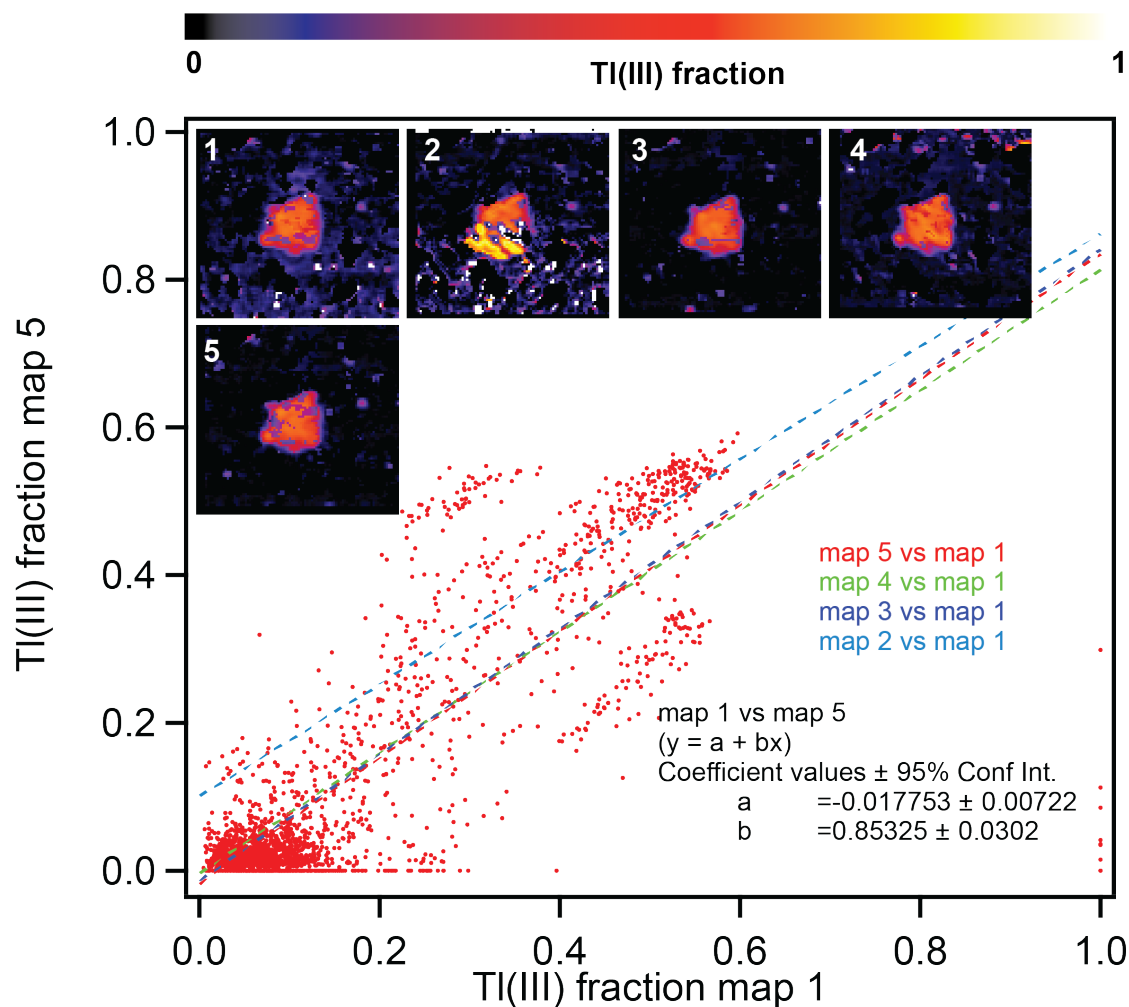
Figure S12: Tl(III) fraction for one concretion where the chemical imaging was repeated 5 times with a total irradiation time of ~5 seconds per pixel (slightly greater due to partial beam overlap in adjacent pixels). The small images show the consecutive maps, after allignment, whereas the big graph shows the correlation of pixels between the first map and the last map, and linear regression for the correlation of all 4 maps to the first map (excluding the plot of all points for viewing purposes). Map 2 had an issue in sample moving, resulting in noise in the data (reflected in the linear regression). The lack of a decreasing trend in Tl(III) with time, despite the scatter within the datapoints, suggests that beam damage was not observed.

REFERENCES

Guizar-Sicairos, M., Thurman, S.T. and Fienup, J.R. (2008) Efficient subpixel image registration algorithms. **33**, 156-158.

Mosselmans, J.F., Quinn, P.D., Dent, A.J., Cavill, S.A., Moreno, S.D., Peach, A., Leicester, P.J., Keylock, S.J., Gregory, S.R., Atkinson, K.D. and Rosell, J.R. (2009) I18--the microfocus spectroscopy beamline at the Diamond Light Source. *J. Synchrotron Radiat.* **16**, 818-824.

Ravel, B. and Newville, M. (2005) ATHENA, ARTEMIS, HEPHAESTUS: data analysis for X-ray absorption spectroscopy using IFEFFIT. *J. Synchrotron Radiat.* **12**, 537-541.

Stark, P.B. and Parker, R.L. (1995) Bounded-variable least-squares: an algorithm and applications. **10**, 129-129.

Wielinski, J., Marafatto, F.F., Gogos, A., Scheidegger, A., Voegelin, A., Muller, C.R., Morgenroth, E. and Kaegi, R. (2020) Synchrotron hard X-ray chemical imaging of trace element speciation in heterogeneous samples: development of criteria for uncertainty analysis. *J. Anal. Atom. Spectrom.* **35**, 567-579.